Supplementary Information

Coherent pump pulses in Double Electron Electron Resonance Spectroscopy

Claudia E. Tait,[a] and Stefan Stoll,*[a]

1 Additional experimental considerations

1.1 Characterization of the excitation and detection pathways

The spectrometer transfer function was determined through nutation experiments as reported in reference [1]. The nutation experiments were performed using the pulse sequence $t_p - T - \frac{\pi}{2} - \tau - \pi$ with delays $T = 5\,\mu s$ and $\tau = 200\,ns$ and $\frac{\pi}{2}$ and π pulse lengths of 32 ns and 64 ns, respectively. A two-step phase cycle on the first pulse was used. The length of the first pulse, t_p, was varied from 0 to 200 ns in 2 ns increments. The frequency was varied in 10 MHz increments in the range from 33.750 GHz to 34.100 GHz and in 5 MHz increments in the region from 33.840 GHz to 33.970 GHz. The measurements were performed at magnetic fields corresponding to the maximum of the nitroxide spectrum for each sample and under the same conditions as for the DEER and echo transient measurements.

The nutation frequencies ν_1 were determined from the maximum of the magnitude FT spectrum computed after apodization with an exponential window and zero-filling. The resulting resonator profile is shown in Fig. S1. The magnitude transfer function over the whole frequency range was approximated by extending the experimental transfer function with an ideal transfer function of an RLC series circuit [1] with resonance frequency and loaded Q-value Q_L determined by fitting of the experimental data ($\nu_{res} = 33.904\,GHz$, $Q_L = 272$). The imaginary part of the transfer function was computed by Hilbert transform. [1]

The video amplifier after the mixer in the spectrometer's detection pathway is characterized by a non-flat frequency response in the band of interest. [2] Therefore, the frequency response for a video bandwidth set to 200 MHz and a series of different video gain settings (0, 12, 24, 30, 36, 42 and 48 dB) was measured by connecting the AWG output to the video amplifier input, programming a 1 µs rectangular pulse at frequencies varying in the range from 0 MHz to 200 MHz with 1 MHz increments and recording the output (10 averages). The input signal amplitude was adjusted to give approximately the same output amplitude for each of the video gain settings; this output amplitude was comparable to the amplitude of the recorded echo signals. The amplitude at each frequency was determined by fitting with a cosine function. The resulting frequency response was divided by the result of a reference measurement of the AWG output. The resulting frequency response functions for different video gain settings are shown in Fig. S2.

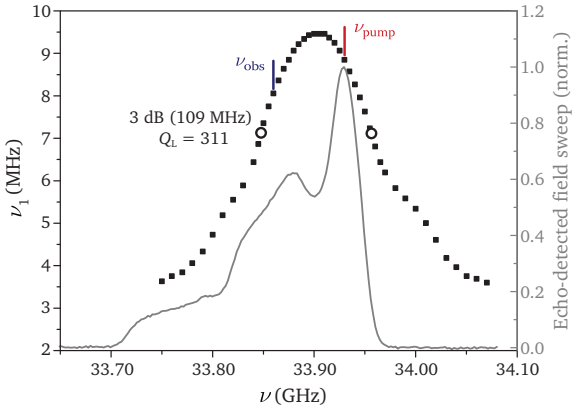

Fig. S1 Plot of the resonator profile determined using nutation experiments. The 3 dB points are highlighted and the loaded Q-value Q_L calculated as the ratio of the centre frequency and 3 dB bandwidth is given. The observer and pump frequencies are indicated by the blue and red line, respectively. A nitroxide echo-detected field sweep converted to a frequency axis is shown for comparison. The shown resonator profile corresponds to the conditions used for the recording of the echo transients shown in the main text.

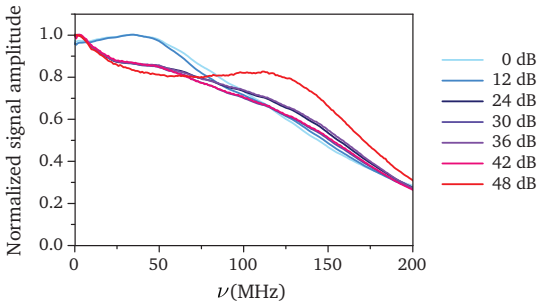

Fig. S2 Frequency response of the video amplifier set to a video bandwidth of 200 MHz and different video gain settings. The frequency response was measured experimentally as described in the text.

[a] *Department of Chemistry, University of Washington, Seattle, WA 98195, USA.*
* Corresponding author. E-mail: stst@uw.edu

1.2 Optimization of the sech/tanh pulse parameters

The amplitude and frequency modulation functions of a sech/tanh pulse are given by:[4]

$$B_1(t) = B_1^{\max}\mathrm{sech}(\beta t) \quad (1)$$

$$\nu(t) = \frac{1}{2}BW_\infty \tanh(\beta t) \quad (2)$$

where $B_1^{\max}$ is the maximum B_1 field, β is a truncation parameter, BW_∞ is the pulse bandwidth for $\tanh(\beta t)$ (the pulse sweeps over the range $\pm BW_\infty/2$) and t is defined in the range from $-t_p/2$ to $+t_p/2$. The pulse length of the sech/tanh was chosen to be approximately equal to $t_{dip}/4$, where t_{dip} is the dipolar evolution period corresponding to the expected inter-spin distance. This was shown to be the longest pulse length that would not lead to significant distortions of the DEER trace.[1] Due to the limited power, the longest possible pulse length was chosen and the pulse amplitude was set to full scale. For the four-pulse DEER experiments on a sample with a 3.5 nm inter-spin distance (HCN2-Trip8b$_{core}$ complex doubly spin-labelled on HCN2 at residues S563C and R635C[5]) a 200 ns sech/tanh pump pulse was used. The five- and seven-pulse DEER experiments were performed on a sample with a longer main inter-spin distance of about 4.4 nm (HCN2-Trip8b$_{core}$ complex doubly spin-labelled on HCN2 at residues V537C and R635C[5]) to allow an increase of the pulse length to 400 ns without introducing too significant distortions to the DEER trace.

The pulse parameters for the sech/tanh pump pulse were determined using the optimization method described in reference[3]: $\eta_{2P} = \lambda_{2P}V(0) = V(0) - V(t_r)$ was calculated for pump pulses with different frequency offsets $\Delta\nu$ with respect to a fixed observer frequency, bandwidths BW_∞ and β parameters by recording two points of the DEER trace, $V(0)$ at time $t_{DEER} = 0$ and $V(t_{DEER,r})$ at a later time. A set of parameters maximizing the modulation depth λ_{2P} without significant excitation bandwidth overlap was chosen, resulting in the pump pulse parameters $\Delta\nu = 75$ MHz, $BW_\infty = 70$ MHz and $\beta = 4/t_p$ used for the four-pulse DEER measurements reported here.

For the pump pulse optimization of five- and seven-pulse DEER, further experiments were performed to determine the dependence of the pulse inversion efficiency on the different pulse parameters. The echo intensity for an inversion recovery sequence was recorded as a function of the offset of the sech/tanh pulse centre frequency for a range of different pulse lengths, BW_∞ and β parameters. Pulse parameters leading to the largest uniform inversion of spins within the excitation bandwidth were chosen and further optimized using the same method as for the four-pulse DEER pump pulse optimization. The final pump pulse parameters were $t_p = 400$ ns, $\Delta\nu = 60$ MHz, $BW_\infty = 35$ MHz and $\beta = 6/t_p$.

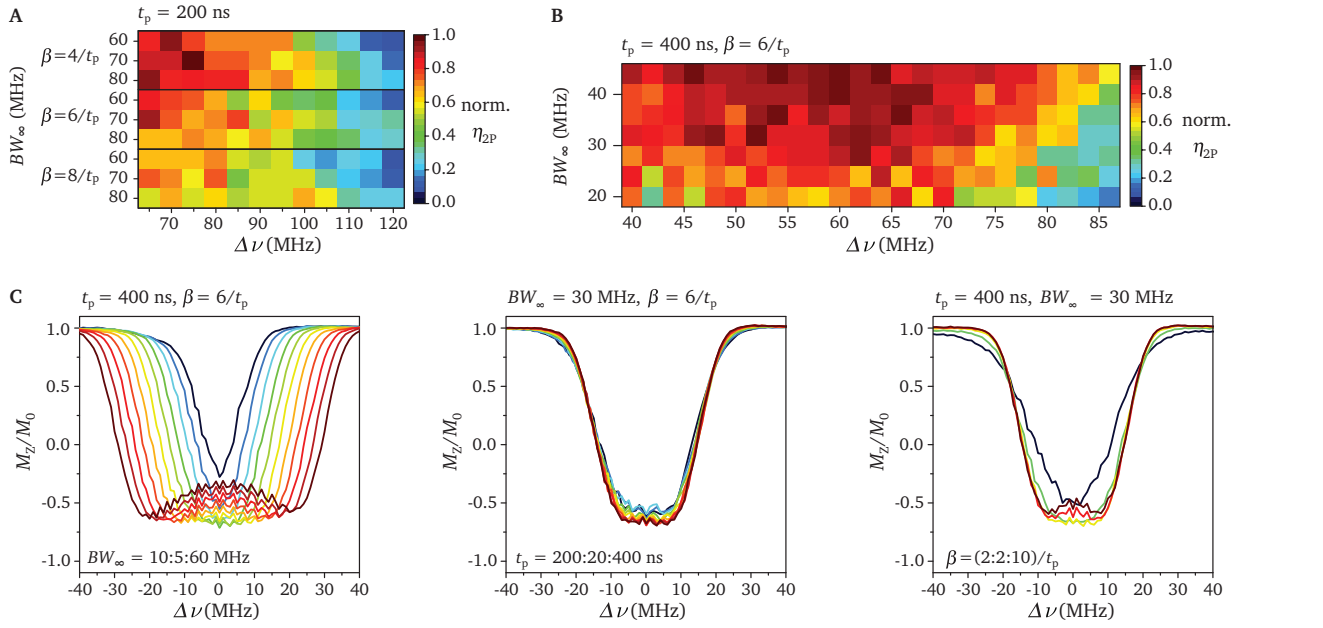

Fig. S3 (**A**) Four-pulse DEER pump pulse optimization experiments. The normalized intensity of the η_{2P} parameter (see reference[3]) is shown as a function of the frequency offset $\Delta\nu$, bandwidth BW_∞ and β parameter of a 200 ns sech/tanh pulse. η_{2P} was calculated as $V(0) - V(t_{DEER,r})$, *i.e.* as the difference in intensity between the DEER echo at time zero and at a later time $t_{DEER,r} = 1$ µs. (**B**,**C**) Five- and seven-pulse DEER pump pulse optimization experiments. The normalized intensity of the η_{2P} parameter is shown as a function of frequency offset $\Delta\nu$ and bandwidth BW_∞ of a 400 ns sech/tanh pulse in **B**. The echo intensity for an inversion recovery sequence at the centre frequency of the resonator dip (*inversion pulse* $-T - \frac{\pi}{2} - \tau - \pi - \tau$, $T = 5$ µs, $\tau = 200$ ns) is shown in **C** as a function of the frequency offset of sech/tanh pulses with different bandwidths BW_∞ (left), different pulse lengths t_p (middle) and different values of the truncation parameter β (right).

2 Echo simulations

2.1 Pulse excitation profiles

The pulse excitation profiles calculated for the pulses used in the echo simulations, *i.e.* rectangular 32 ns $\frac{\pi}{2}$ and 64 ns π pulses at the observer frequency and a rectangular 64 ns π pulse or a 200 ns sech/tanh inversion pulse at frequency offsets of 70 MHz and 75 MHz, respectively, are compared in Fig. S4 A and B. The pulse excitation profiles calculated for Gaussian observer pulses with a 80 ns and 160 ns pulse length and a 32 ns and 64 ns full width at half maximum (FWHM) for $\frac{\pi}{2}$ and π pulses, respectively, are compared with the excitation profile of the sech/tanh inversion pulse at a frequency offset of 75 MHz in Fig. S4 C. The pulse excitation profile calculations were performed by taking the experimental power levels and the spectrometer transfer function into account. The less-than-full inversion by the sech/tanh pulse was due to the limited amount of power.

As an experimental measure of the inversion efficiency for different frequency offsets, the intensity of the echo in an inversion recovery sequence was recorded as a function of frequency offset of the initial inversion pulse for both the 64 ns monochromatic rectangular pulse and the 200 ns sech/tanh pulse used in the DEER experiments.[1] The results are compared in Fig. S5. The result for the sech/tanh pulse is compared to a simulation of its inversion profile. Even though the sech/tanh pulse used is not adiabatic and does not achieve full inversion, the effect of this pulse on spins over a wide bandwidth leads to a significant increase in modulation depth in the DEER experiment with respect to a monochromatic rectangular pulse (see Fig. 6 in the main article).

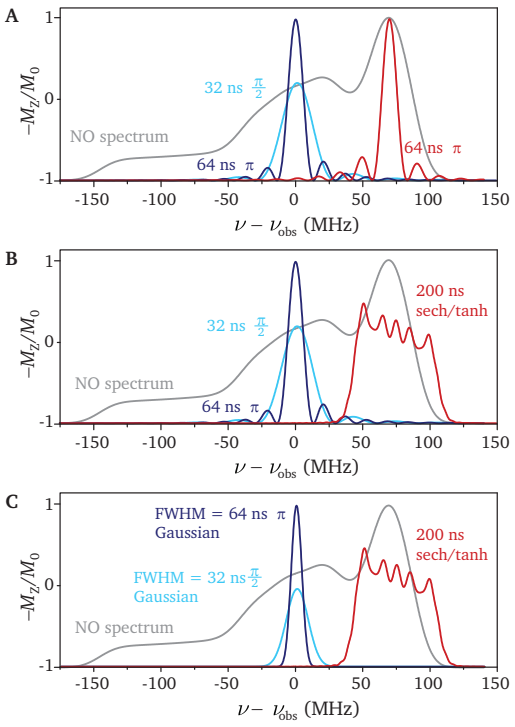

Fig. S4 Simulated pulse excitation profiles (M_z/M_0) for the pulses in a DEER sequence with rectangular (**A** and **B**) or Gaussian (**C**) observer pulses and a rectangular (**A**) or sech/tanh (**B** and **C**) pump pulse. The pulse parameters are the following: rectangular $\frac{\pi}{2}$ and π observer pulses with pulse lengths of 32 ns and 64 ns, Gaussian $\frac{\pi}{2}$ and π observer pulses with 80 ns and 160 ns pulse lengths and 32 ns and 64 ns full widths at half maximum (FWHM), rectangular pump pulse with 64 ns pulse length and a frequency offset of $\Delta\nu = 70$ MHz, sech/tanh pump pulse with $BW_\infty = 70$ MHz, $\beta = 4/t_p$ and a frequency offset of $\Delta\nu = 75$ MHz. The excitation profiles are compared to a simulation of a Q-band nitroxide spectrum.

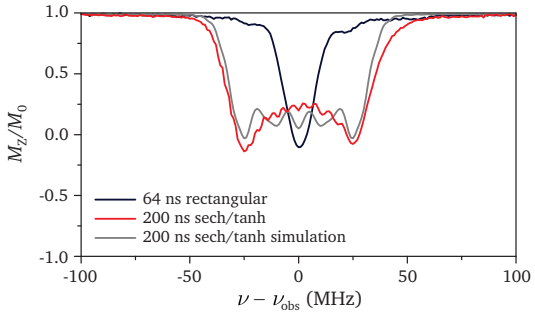

Fig. S5 Echo intensity at the end of an inversion recovery sequence (inversion pulse $-T - \frac{\pi}{2} - \tau - \pi - \tau$, $T = 1\,\mu s$, $\tau = 200$ ns) as a function of the frequency offset of a 64 ns rectangular pulse or the 200 ns sech/tanh pulse used in the DEER experiments. The detection sequence was at $\nu_{obs} = 33.860$ GHz and $B_0 = 1208.9$ mT. The centre frequency of the inversion pulse was varied in the range ± 100 MHz with 1 MHz increments. The calculated excitation profile for the sech/tanh pulse is shown in grey for comparison.

2.2 Fourier transforms of echoes generated by coherent pump pulses

The Fourier transforms of the two- and three-pulse echoes generated by different combinations of monochromatic rectangular observer pulses and rectangular or sech/tanh pump pulses, shown in Fig. 4 in the main article, are shown in Fig. S7.

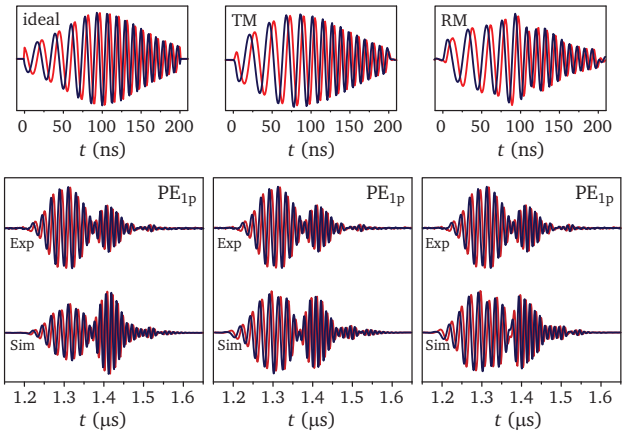

Fig. S6 Experimentally recorded echo generated by a 32 ns $\frac{\pi}{2}$ pulse at ν_{obs} (33.83 GHz) and a sech/tanh pulse ($t_p = 200$ ns, $BW_\infty = 70$ MHz, $\beta = 4/t_p$) centred at an offset frequency $\Delta\nu = +75$ MHz (top trace, bottom panel) and corresponding simulations (bottom trace, bottom panel) performed for an ideal sech/tanh pulse, the sech/tanh pulse recorded using the spectrometer's transmitter mode (TM) and receiver mode (RM). The corresponding pulse shapes are shown in the top panel.

A Fourier transforms of observer sequence echoes

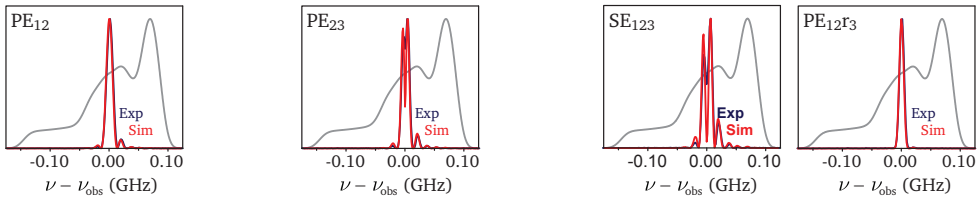

B Fourier transforms of additional echoes for a coherent rectangular pulse at the pump frequency

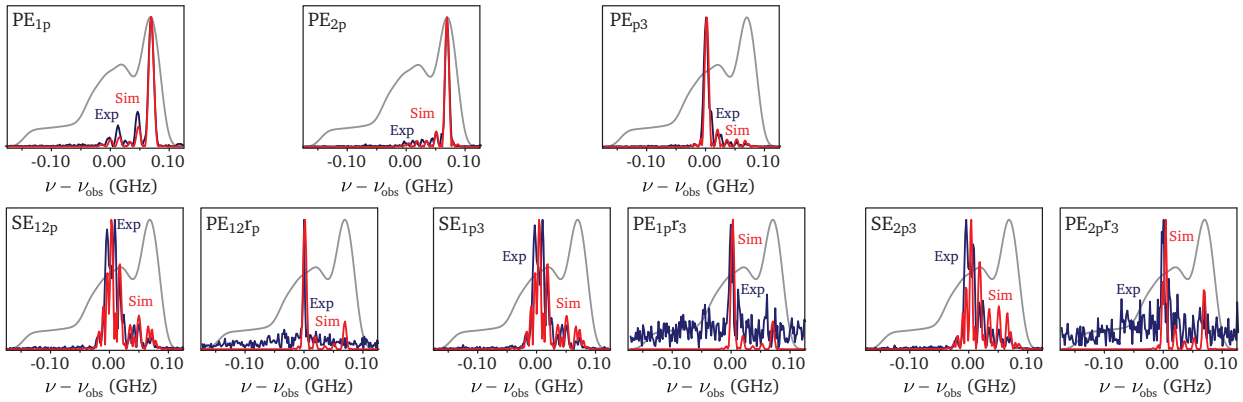

C Fourier transforms of additional echoes for a coherent sech/tanh pulse at the pump frequency

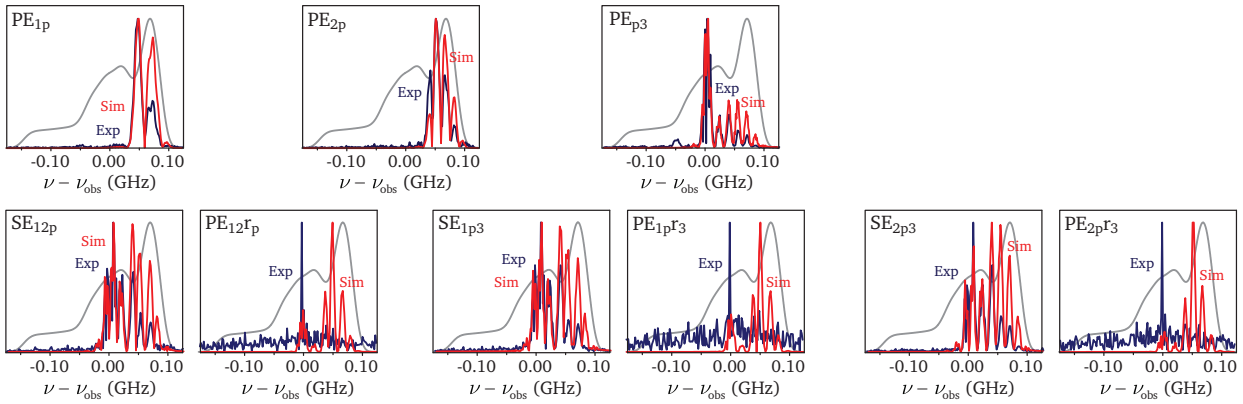

Fig. S7 Fourier transforms of the experimental (blue) and simulated (red) two- and three-pulse echoes generated by 32 ns and 64 ns rectangular $\frac{\pi}{2}$ and π pulses at the observer frequency (**A**), by rectangular pulses at the observer frequency and a 64 ns rectangular π pulse at a coherent pump frequency ($\Delta\nu = +70$ MHz) (**B**) and by rectangular pulses at the observer frequency and a 200 ns sech/tanh pulse ($BW_\infty = 70$ MHz, $\beta = 4/t_p$) at a coherent pump frequency ($\Delta\nu = +75$ MHz) (**C**). The echoes are labelled as in Table 1, where 1, 2 and 3 stand for the first ($\frac{\pi}{2}$), second (π) and third (π) observer pulse of a four-pulse DEER sequence, respectively. The corresponding echoes are shown in Figure4 of the main text.

2.3 Pulse distortions

As discussed in the main text, the experimental echo transients, especially for sequences containing sech/tanh pulses, showed a lower weighting of the contributions at higher frequencies compared to the corresponding simulations. One of the possible reasons for this discrepancy is a distortion of the pulses in the transmitter. This was investigated by recording the experimental sech/tanh pulse shapes in the transmitter mode (bypassing up-conversion, amplification, resonator and receiver front end) and receiver mode (bypassing the protection switch and X-band LNA) of the spectrometer (see SI Fig. S6). The amplitude function of both recorded pulses decays towards higher frequencies and the relative intensities of different frequencies contributing to echoes simulated using the experimental pulse shapes approach those observed experimentally.

2.4 Echoes for Gaussian observer pulses

The full set of two- and three-pulse echoes with Gaussian observer pulses and the corresponding Fourier transforms are shown in Fig. S8.

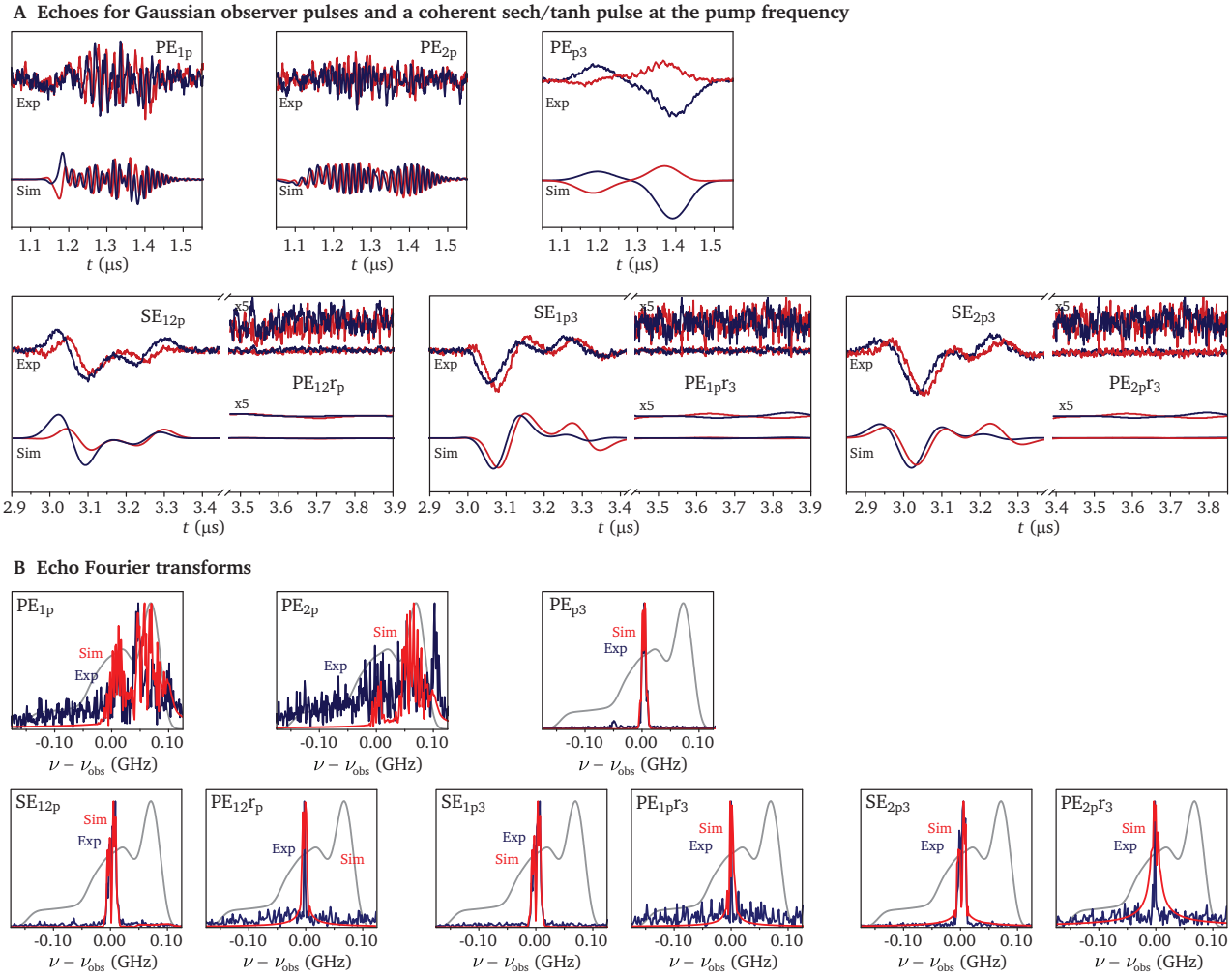

Fig. S8 Experimental (top) and simulated (bottom) two- and three-pulse echoes (**A**) and the corresponding Fourier transforms (**B**) obtained from sequences with Gaussian observer pulses, with pulse lengths of 80 ns and 160 ns and FWHM of 32 ns and 64 ns for $\frac{\pi}{2}$ and π pulses, respectively, and a 200 ns sech/tanh pulse ($BW_\infty = 70$ MHz, $\beta = 4/t_p$) at a coherent pump frequency ($\Delta\nu = +75$ MHz). The echoes are labelled as in Table 1, where 1, 2 and 3 stand for the first ($\frac{\pi}{2}$), second (π) and third (π) observer pulse of a four-pulse DEER sequence, respectively. Two-pulse echoes were recorded and simulated with a delay τ equal to 600 ns, three-pulse echoes with a first delay of 600 ns and a second delay of 1800 ns. The simulations were performed as described in the main text and the time axis, intensity and phase was adjusted individually to match the experiment.

2.5 Relative echo intensities

The relative intensities under different experimental conditions of echoes generated by three-pulse sequences, where one of the refocusing pulses is replaced by a pulse at a different frequency, were analysed by performing simulations using the same procedure as described in section 5.3 of the main text. A 200 ns sech/tanh pulse with a bandwidth BW_∞ of 70 MHz and a β parameter of $4/t_p$ was used for the simulations. The pulse amplitudes were adjusted to obtain flip angles of $\frac{\pi}{2}$, π and π for the three pulses of the sequence.[6]

The observer pulse lengths or the frequency offset between observer and pump frequencies were varied to determine the changes in relative echo intensities for decreasing extents of excitation bandwidth overlap. The results of the simulations are shown in Fig. S9. The echo simulations show that, in the presence of significant overlap between the excitation bandwidths of the observer and pump pulses, the intensity of the refocused echo can become comparable to the intensity of the stimulated echo, while for small excitation bandwidth overlap the refocused echo intensity can become an order of magnitude smaller compared to the corresponding stimulated echo.

The integrated echo intensities of the three primary echoes, the stimulated and the refocused echoes (normalized to give unitary integral for the primary echo PE_{12}) are compared in the panels on the right of Fig. S9. A comparison of the normalized integrated intensities of the stimulated and refocused echoes with the normalized overlap integral of the excitation profiles of the two-pulse primary echo sequence and of the sech/tanh pulse shows that the integrated intensity of the refocused echo is approximately proportional to the excitation profile overlap and decays relatively quickly as the observer pulse length or the frequency offset is increased. The integrated intensity of the stimulated echo however decays much more slowly and the stimulated echo still exhibits considerable intensity (ca. 10% of the intensity of the PE_{12} echo) even for a very small overlap of the excitation profiles of the corresponding pulses. Since the simulations were performed without taking relaxation into account, experimentally the echo intensities of the stimulated (at $T+2\tau$), the refocused (at $2T$) and the two primary echoes (at $2T+\tau$ and $2T+2\tau$) with respect to the echo intensity of the first primary echo PE_{12} (at 2τ) are expected to be progressively decreased due to relaxation during the different delays up to the point of refocusing.

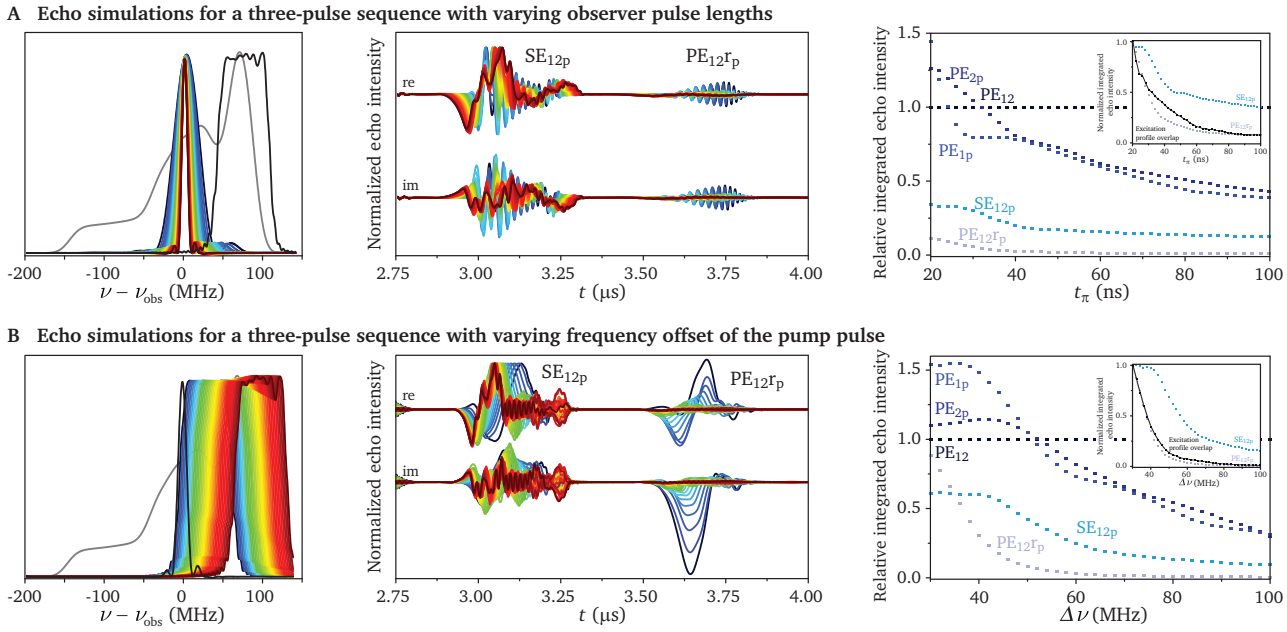

Fig. S9 Excitation profiles of the initial two-pulse sequence and of the sech/tanh pulse (left), stimulated and refocused echo simulations (middle, normalized to the maximum intensity of the stimulated echo) and integrated echo intensities (right) as a function of observer pulse lengths ranging from t_π = 20-100 ns ($t_{\frac{\pi}{2}}$ = 10-50 ns, blue to red) (**A**) and as a function of the frequency offset between observer and pump frequency ranging from $\Delta\nu$ = 30-100 MHz (blue to red) (**B**). The simulations are performed for a three-pulse sequence with $\frac{\pi}{2}$ and π monochromatic rectangular observer pulses and a 200 ns sech/tanh pulse with a bandwidth BW_∞ of 70 MHz and a β parameter of $4/t_p$. For (**A**) the central frequency offset for the pump pulse was set to 75 MHz and the observer pulse length was varied; for (**B**) the observer pulse lengths were set to 32 ns and 64 ns for the $\frac{\pi}{2}$ and π pulses, respectively, and the central frequency offset of the pump pulse was varied. The inter-pulse delays were 600 ns (τ) and 1800 ns (T). For the comparison of integrated echo intensities, the calculated signal was normalized by division with the integral of the primary echo PE_{12}. The normalized integrated intensities for the stimulated and refocused echo are compared to the normalized integral of the pulse excitation profile overlap in the insets.

3 Four-pulse DEER

3.1 Four-pulse DEER under different experimental conditions

The dependence of the intensity of the echo crossing artefacts on the experimental conditions of the DEER experiment was investigated by decreasing the excitation bandwidth overlap by either increasing the frequency offset between observer and pump frequencies or by using Gaussian observer pulses.

Four-pulse DEER traces recorded with rectangular observer pulses and a sech/tanh pump pulse at central frequency offsets of 75 MHz and 95 MHz are compared in Fig. S10. The intensity of the echo-crossing artefacts is much reduced for the trace recorded with the larger frequency offset, but they are still present, as can be seen particularly well in the quadrature part of the trace. Since the observer frequency was shifted away from the centre of the resonator dip to increase $\Delta\nu$, the echo intensity for the DEER experiment with the larger frequency offset was smaller, as reflected by the decreased signal-to-noise ratio of that trace.

A four-pulse DEER trace recorded with Gaussian observer pulses is compared to the trace recorded with rectangular observer pulses in Fig. S11. Echo transients recorded for two pump pulse positions are also shown for both types of observer pulses. The echo transients show that the intensity of the crossing primary echoes is reduced almost to the noise level for Gaussian observer pulses, however the stimulated and delayed echoes still have sufficient intensity to lead to visible distortions of the DEER trace.

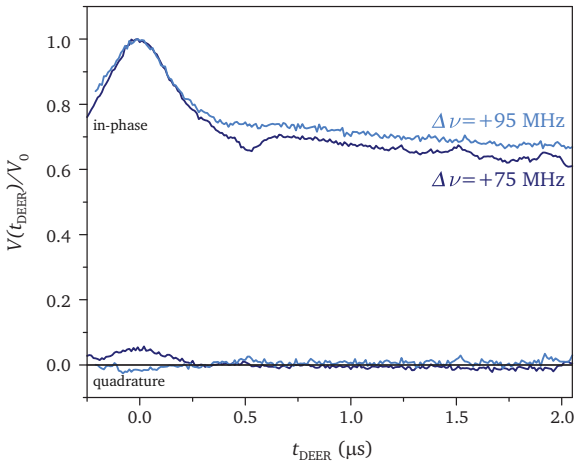

Fig. S10 Comparison of the in-phase (top) and quadrature (bottom) parts of four-pulse DEER traces recorded with a coherent 200 ns sech/tanh pump pulse at frequency offsets of $\Delta\nu = 75$ MHz and $\Delta\nu = 95$ MHz without phase cycling. The two measurements were performed at observer frequencies of 33.860 GHz and 33.840 GHz, respectively. The magnetic field was set to 1208.9 mT, corresponding to the maximum of the nitroxide spectrum at the central pump frequency, in both cases. Additional experimental details are given in section 5.

3.2 Phase cycles for four-pulse DEER

The efficiency of the different types of phase cycles described for four-pulse DEER (see Table 2 in the main text) is visualized in Fig. S12.

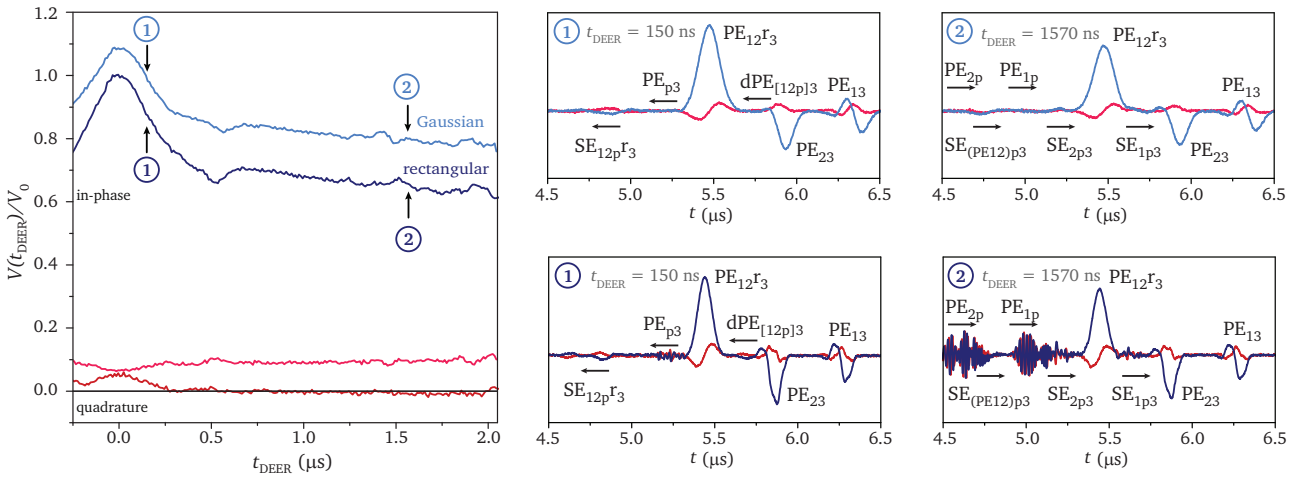

Fig. S11 Comparison of the in-phase (top) and quadrature (bottom) parts of four-pulse DEER traces recorded with rectangular and Gaussian observer pulses (pulse lengths of 80 ns and 160 ns and FWHM of 32 ns and 64 ns for $\frac{\pi}{2}$ and π pulses, respectively) and a 200 ns sech/tanh pump pulse at a frequency offset of $\Delta\nu = 75$ MHz without phase cycling ($\nu_{obs} = 33.83$ GHz, $B_0 = 1207.9$ mT, $\tau_1 = 400$ ns, $\tau_2 = 2.3$ µs, further details in the experimental section). The echo transients recorded for two positions of the coherent sech/tanh pump pulse are shown on the right for the Gaussian observer pulses (top) and the rectangular observer pulses (bottom). The different echoes are labelled according to Table 1 and the direction of movement for crossing echoes is indicated by arrows.

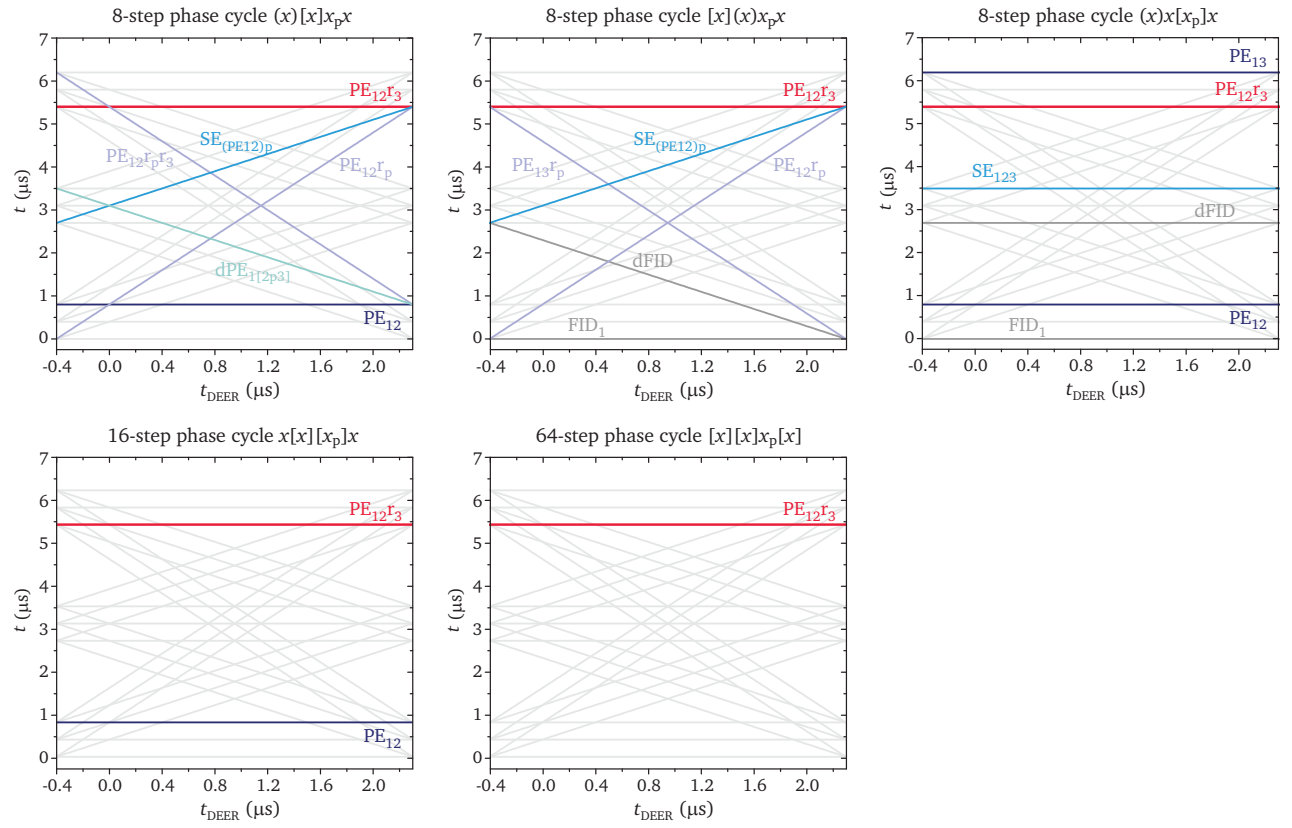

Fig. S12 Visualization of the echoes removed in different phase cycles for the four-pulse DEER sequence. The positions of the echo crossings in a four-pulse DEER experiment with $\tau_1 = 400$ ns and $\tau_2 = 2.3$ µs are shown as in Fig. 3. The lines corresponding to echoes removed by the phase cycle are shown in grey, the detected echo is shown in red and the echoes not removed by phase cycling are shown in different shades of blue depending on the type of echo and are labelled according to Table 1.

4 Multi-pump-pulse DEER

4.1 Five-pulse DEER

The different echoes generated in a five-pulse DEER sequence with two coherent pump pulses, the corresponding coherence transfer pathways, the echo positions and crossing times are reported in Tables S2 and S1 for the reverse and forward five-pulse experiment, respectively.

The efficiency of the different types of phase cycles described for the two versions of the five-pulse DEER (see Table 2 in the main text) is visualized in Fig. S14 and Fig. S15.

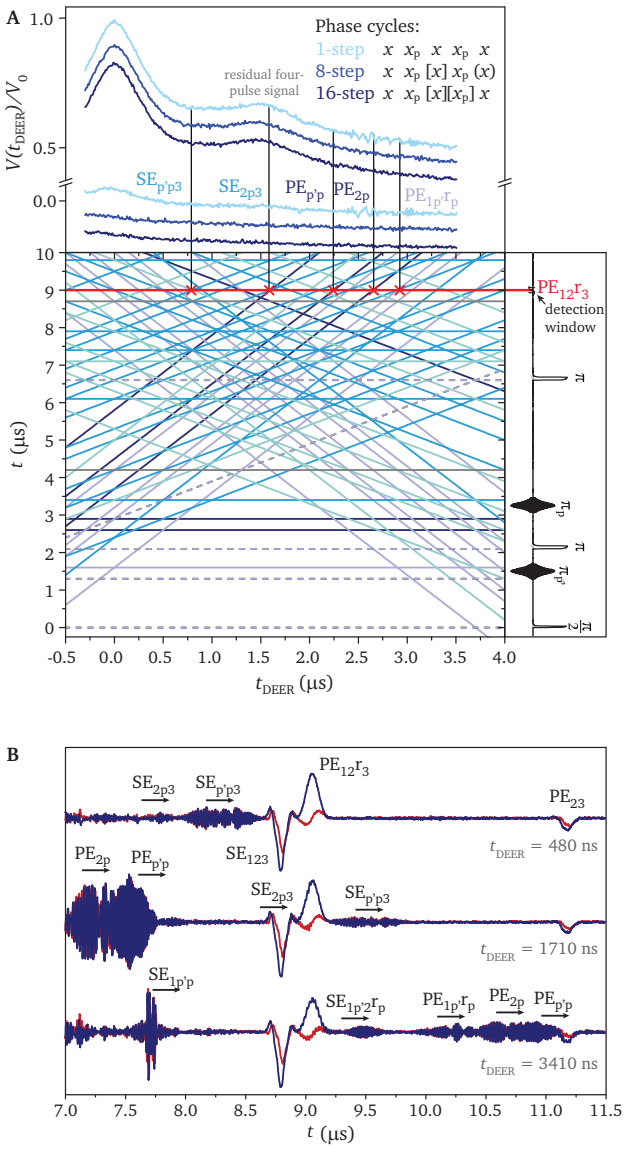

Fig. S13 (**A**) Positions of the echo crossings in the forward five-pulse DEER experiment with the following inter-pulse delays $\tau_1 = 2.1\,\mu s$, $\tau_2 = 2.4\,\mu s$ and $t_2 = 800\,ns$. The pulse sequence is plotted along the y-axis with pulse positions represented by dashed lines. The standing echoes of the observer sequence are shown in grey and the different types of echoes induced by the pump pulses are shown in different shades of blue following the same colour code as in Fig. 3. Five-pulse DEER traces recorded with different phase cycles are shown in the top panel (The traces are offset to allow better comparison.). The crossing positions of the most intense moving echoes with the detected refocused echo ($PE_{12}r_3$, position shown in red) are highlighted and tentatively assigned. (**B**) Echo transients recorded for three positions of the moving pump pulse. The different echoes are labelled according to Table S1 and the direction of movement for crossing echoes is indicated by arrows.

Table S1 Echoes, coherence transfer pathways, positions and crossing times $t_{\mathrm{DEER,cross}}$ with the refocused echo ($\mathrm{PE_{12}r_3}$) for forward five-pulse DEER. (PE = primary echo, SE = stimulated echo, r = refocused, d = delayed). The time axis of the DEER experiment is given by $t_{\mathrm{DEER}} = t_1 - t_2$.

Echo	Pathway					Position	$t_{\mathrm{DEER,cross}}$
$\mathrm{PE_{1p'}}$	+	−	−	−	−	$2\tau_1 - 2t_2$	-
$\mathrm{PE_{12}}$	+	+	−	−	−	$2\tau_1$	-
$\mathrm{PE_{p'2}}$	0	+	−	−	−	$\tau_1 + t_2$	-
$\mathrm{PE_{1p}}$	+	+	+	−	−	$2\tau_1 + 2t_1$	-
$\mathrm{PE_{p'p}}$	0	+	+	−	−	$\tau_1 + 2t_1 + t_2$	$\frac{1}{2}\tau_1 + \tau_2 - \frac{3}{2}t_2$
$\mathrm{PE_{2p}}$	0	0	+	−	−	$\tau_1 + 2t_1$	$\frac{1}{2}\tau_1 + \tau_2 - t_2$
$\mathrm{PE_{13}}$	+	+	+	+	−	$4\tau_1 + 2\tau_2$	-
$\mathrm{PE_{p'3}}$	0	+	+	+	−	$3\tau_1 + 2\tau_2 + t_2$	-
$\mathrm{PE_{23}}$	0	0	+	+	−	$3\tau_1 + 2\tau_2$	-
$\mathrm{PE_{p3}}$	0	0	0	+	−	$3\tau_1 + 2\tau_2 - t_1$	$\tau_1 - t_2$
$\mathrm{PE_{1p'}r_2}$	−	+	−	−	−	$2t_2$	-
$\mathrm{PE_{1p'}r_p}$	−	+	+	−	−	$2(t_1 + t_2)$	$\tau_1 + \tau_2 - 2t_2$
$\mathrm{PE_{1p'}r_3}$	−	+	+	+	−	$2(\tau_1 + \tau_2 + t_2)$	-
$\mathrm{PE_{12}r_p}$	−	−	+	−	−	$2t_1$	$\tau_1 + \tau_2 - t_2$
$\mathrm{PE_{12}r_3}$	−	−	+	+	−	$2(\tau_1 + \tau_2)$	
$\mathrm{PE_{13}r_{p'}}$	−	−	−	+	−	$2t_2$	-
$\mathrm{PE_{p'2}r_p}$	0	−	+	−	−	$\tau_1 + 2t_1 - t_2$	$\frac{1}{2}\tau_1 + \tau_2 - \frac{1}{2}t_2$
$\mathrm{PE_{p'2}r_3}$	0	−	+	+	−	$3\tau_1 + 2\tau_2 - t_2$	-
$\mathrm{PE_{p'p}r_3}$	0	−	−	+	−	$3\tau_1 + 2\tau_2 - 2t_1 - t_2$	$\frac{1}{2}\tau_1 - \frac{3}{2}t_2$
$\mathrm{PE_{2p}r_3}$	0	0	−	+	−	$3\tau_1 + 2\tau_2 - 2t_1$	$\frac{1}{2}\tau_1 - t_2$
$\mathrm{PE_{1p'}r_2r_p}$	+	−	+	−	−	$2(\tau_1 + t_1)$	τ_2
$\mathrm{PE_{1p'}r_2r_3}$	+	−	+	+	−	$2(2\tau_1 + \tau_2 - t_2)$	-
$\mathrm{PE_{1p'}r_pr_3}$	+	−	−	+	−	$2(2\tau_1 + \tau_2 - t_1 - t_2)$	$\tau_1 - 2t_2$
$\mathrm{PE_{12}r_pr_3}$	+	+	−	+	−	$2(2\tau_1 + \tau_2 - t_1)$	$\tau_1 - t_2$
$\mathrm{PE_{p'2}r_pr_3}$	0	+	−	+	−	$3\tau_1 + 2\tau_2 - 2t_1 + t_2$	$\frac{1}{2}\tau_1 - \frac{1}{2}t_2$
$\mathrm{PE_{1p'}r_2r_pr_3}$	−	+	−	+	−	$2(\tau_1 + \tau_2 - t_1 + t_2)$	0
$\mathrm{dPE_{1[p'2p]}}$	+	−	0	−	−	$2\tau_1 + t_1 - 2t_2$	$2\tau_2 + t_2$
$\mathrm{dPE_{[1p'2]p}}$	+	0	+	−	−	$2\tau_1 + 2t_1 - t_2$	$\tau_2 - \frac{1}{2}t_2$
$\mathrm{dPE_{1[p'23]}}$	+	−	0	0	−	$3\tau_1 + \tau_2 - 2t_2$	-
$\mathrm{dPE_{[1p'2]3}}$	+	0	+	+	−	$4\tau_1 + 2\tau_2 - t_2$	-
$\mathrm{dPE_{1[p'\ p3]}}$	+	−	−	0	−	$3\tau_1 + \tau_2 - t_1$	$\tau_1 - \tau_2 - t_2$
$\mathrm{dPE_{[1p'\ p]3}}$	+	0	0	+	−	$4\tau_1 + 2\tau_2 - t_1 - t_2$	$2\tau_1 - 2t_2$
$\mathrm{dPE_{1[2p3]}}$	+	+	−	0	−	$3\tau_1 + \tau_2 - t_1$	$\tau_1 - \tau_2 - t_2$
$\mathrm{dPE_{[12p]3}}$	+	+	0	+	−	$4\tau_1 + 2\tau_2 - t_1$	$2\tau_1 - t_2$
$\mathrm{dPE_{p'[2p3]}}$	0	+	−	0	−	$2\tau_1 + \tau_2 - t_1 + t_2$	$-\tau_2$
$\mathrm{dPE_{[p'2p]3}}$	0	+	0	+	−	$3\tau_1 + 2\tau_2 - t_1 + t_2$	τ_1
$\mathrm{dPE_{[1p'2]p}r_3}$	−	0	−	+	−	$2\tau_1 + 2\tau_2 - 2t_1 + t_2$	$-\frac{1}{2}t_2$
$\mathrm{dPE_{1[p'2p]}r_3}$	−	+	0	+	−	$2\tau_1 + 2\tau_2 - t_1 + 2t_2$	t_2
$\mathrm{dPE_{1p'r_{[2p3]}}}$	−	+	−	0	−	$\tau_1 + \tau_2 - t_1 + 2t_2$	$-\tau_1 - \tau_2 + t_2$
$\mathrm{SE_{1p'2}}$	+	0	−	−	−	$2\tau_1 - t_2$	-
$\mathrm{SE_{1p'p}}$	+	0	0	−	−	$2\tau_1 + t_1 - t_2$	$2\tau_2$
$\mathrm{SE_{1p'3}}$	+	0	0	0	−	$3\tau_1 + \tau_2 - t_2$	-
$\mathrm{SE_{12p}}$	+	+	0	−	−	$2\tau_1 + t_1$	$2\tau_2 - t_2$
$\mathrm{SE_{123}}$	+	+	0	0	−	$3\tau_1 + \tau_2$	-
$\mathrm{SE_{1p3}}$	+	+	+	0	−	$3\tau_1 + \tau_2 + t_1$	$-\tau_1 + \tau_2 - t_2$
$\mathrm{SE_{p'2p}}$	0	+	0	−	−	$\tau_1 + t_1 + t_2$	$\tau_1 + 2\tau_2 - 2t_2$
$\mathrm{SE_{p'23}}$	0	+	0	0	−	$2\tau_1 + \tau_2 + t_2$	-
$\mathrm{SE_{p'\ p3}}$	0	+	+	0	−	$2\tau_1 + \tau_2 + t_1 + t_2$	$\tau_2 - 2t_2$
$\mathrm{SE_{2p3}}$	0	0	+	0	−	$2\tau_1 + \tau_2 + t_1$	$\tau_2 - t_2$
$\mathrm{SE_{1p'2}r_p}$	−	0	+	−	−	$2t_1 + t_2$	$\tau_1 + \tau_2 - \frac{3}{2}t_2$
$\mathrm{SE_{1p'p}r_3}$	−	0	0	+	−	$2\tau_1 + 2\tau_2 - t_1 + t_2$	0
$\mathrm{SE_{1p'2}r_3}$	−	0	+	+	−	$2\tau_1 + 2\tau_2 + t_2$	-
$\mathrm{SE_{12p}r_3}$	−	−	0	+	−	$2\tau_1 + 2\tau_2 - t_1$	$-t_2$
$\mathrm{SE_{p'2p}r_3}$	0	−	0	+	−	$3\tau_1 + 2\tau_2 - t_1 - t_2$	$\tau_1 - 2t_2$
$\mathrm{SE_{1p'2}r_pr_3}$	+	0	−	+	−	$4\tau_1 + 2\tau_2 - 2t_1 - t_2$	$\tau_1 - \frac{3}{2}t_2$
$\mathrm{SE_{(PE1p')2p}}$	−	+	0	−	−	$t_1 + 2t_2$	$2\tau_1 + 2\tau_2 - 3t_2$
$\mathrm{SE_{(PE1p')p3}}$	−	+	+	0	−	$\tau_1 + \tau_2 + t_1 + 2t_2$	$\tau_1 + \tau_2 - 3t_2$
$\mathrm{SE_{(PE1p')23}}$	−	+	0	0	−	$\tau_1 + \tau_2 + 2t_2$	-
$\mathrm{SE_{(PE12)p3}}$	−	−	+	0	−	$\tau_1 + \tau_2 + t_1$	$\tau_1 + \tau_2 - t_2$
$\mathrm{SE_{(PEp'2)p3}}$	0	−	+	0	−	$2\tau_1 + \tau_2 + t_1$	τ_2
$\mathrm{SE_{(PE1p')2p}r_3}$	+	−	0	+	−	$4\tau_1 + 2\tau_2 - t_1 - 2t_2$	$2\tau_1 - 3t_2$
$\mathrm{SE_{(PE1p'r2)p3}}$	+	−	+	0	−	$3\tau_1 + \tau_2 + t_1 - 2t_2$	$-\tau_1 + \tau_2 + t_2$
$\mathrm{SE_{(SE1p'2)p3}}$	−	0	+	0	−	$\tau_1 + \tau_2 + t_1 + t_2$	$\tau_1 + \tau_2 - 2t_2$
$\mathrm{dSE_{1p'[2p3]}}$	+	0	−	0	−	$3\tau_1 + \tau_2 - t_1 - t_2$	$\tau_1 - \tau_2 - 2t_2$
$\mathrm{dSE_{[1p'2]p3}}$	+	0	+	0	−	$3\tau_1 + \tau_2 + t_1 - t_2$	$-\tau_1 + \tau_2$

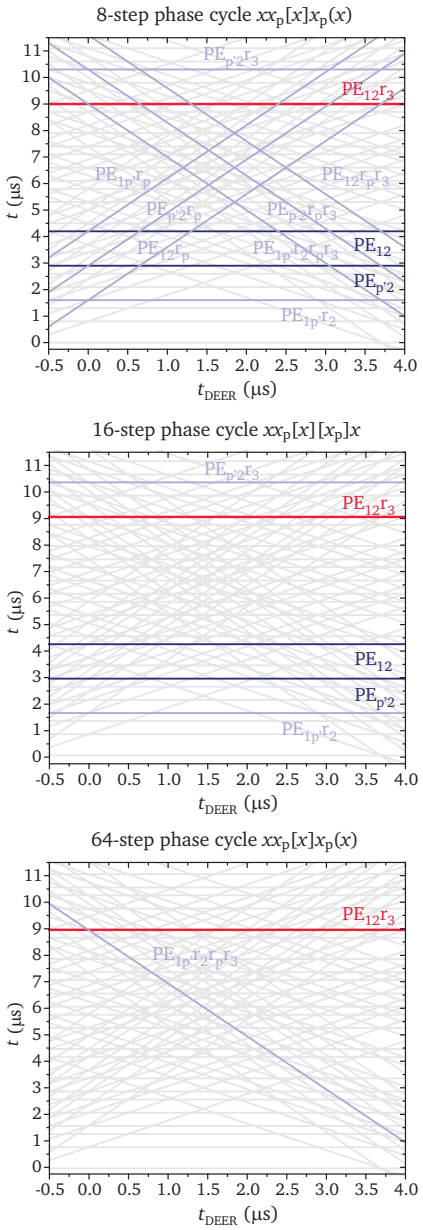

Fig. S14 Visualization of the echoes removed in different phase cycles for forward five-pulse DEER sequence. The positions of the echo crossings in a five-pulse DEER experiment with $\tau_1 = 2.1\,\mu s$, $\tau_2 = 2.4\,\mu s$ and $t_2 = 800\,ns$ are shown as in Fig. S13. The lines corresponding to echoes removed by the phase cycle are shown in grey, the detected echo is shown in red, and the echoes not removed by phase cycling are shown in different shades of blue depending on the type of echo and are labelled according to Table S1.

Table S2 Echoes, coherence transfer pathways, positions and crossing times $t_{DEER,cross}$ with the refocused echo ($PE_{12}r_3$) for reverse five-pulse DEER. (PE = primary echo, SE = stimulated echo, r = refocused, d = delayed). The time axis of the DEER experiment is given by $t_{DEER} = t_1 - t_2$.

Echo	Pathway					Position	$t_{DEER,cross}$
PE_{12}	+	−	−	−	−	$2\tau_1$	-
PE_{1p}	+	+	−	−	−	$4\tau_1+2\tau_2-2t_1$	τ_1-t_2
PE_{2p}	0	+	−	−	−	$3\tau_1+2\tau_2-2t_1$	$\frac{1}{2}\tau_1-t_2$
PE_{13}	+	+	+	−	−	$4\tau_1+2\tau_2$	-
PE_{23}	0	+	+	−	−	$3\tau_1+2\tau_2$	-
PE_{p3}	0	0	+	−	−	$2\tau_1+\tau_2+t_1$	τ_2-t_2
$PE_{1p'}$	+	+	+	+	−	$4\tau_1+2\tau_2+2t_2$	-
$PE_{2p'}$	0	+	+	+	−	$3\tau_1+2\tau_2+2t_2$	-
$PE_{pp'}$	0	0	+	+	−	$2\tau_1+\tau_2+t_1+2t_2$	τ_2-3t_2
$PE_{3p'}$	0	0	0	+	−	$2\tau_1+\tau_2+2t_2$	-
$PE_{12}r_p$	−	+	−	−	−	$2(\tau_1+\tau_2-t_1)$	$-t_2$
$PE_{12}r_3$	−	+	+	−	−	$2(\tau_1+\tau_2)$	
$PE_{12}r_{p'}$	−	+	+	+	−	$2(\tau_1+\tau_2+t_2)$	-
$PE_{1p}r_3$	−	−	+	−	−	$2(t_1+t_2)$	$\tau_1+\tau_2-t_2$
$PE_{1p}r_{p'}$	−	−	+	+	−	$2(t_1+t_2)$	$\tau_1+\tau_2-2t_2$
$PE_{13}r_{p'}$	−	−	−	+	−	$2t_2$	-
$PE_{2p}r_3$	0	−	+	−	−	τ_1+2t_1	$\frac{1}{2}\tau_1+\tau_2-t_2$
$PE_{2p}r_{p'}$	0	−	+	+	−	$\tau_1+2(t_1+t_2)$	$\frac{1}{2}\tau_1+\tau_2-2t_2$
$PE_{23}r_{p'}$	0	−	−	+	−	τ_1+2t_2	-
$PE_{p3}r_{p'}$	0	0	−	+	−	$2\tau_1+\tau_2-t_1+2t_2$	$-\tau_2+t_2$
$PE_{12}r_pr_3$	+	−	+	−	−	$2(\tau_1+t_1)$	τ_2-t_2
$PE_{12}r_pr_{p'}$	+	−	+	+	−	$2(\tau_1+t_1+t_2)$	τ_2-2t_2
$PE_{12}r_3r_{p'}$	+	−	−	+	−	$2(\tau_1+t_2)$	-
$PE_{1p}r_3r_{p'}$	+	+	−	+	−	$4\tau_1+2\tau_2-2t_1+2t_2$	τ_1
$PE_{2p}r_3r_{p'}$	0	+	−	+	−	$3\tau_1+2\tau_2-2t_1+2t_2$	$\frac{1}{2}\tau_1$
$PE_{12}r_pr_3r_{p'}$	−	+	−	+	−	$2\tau_1+2\tau_2-2t_1+2t_2$	0
$dPE_{1[2p3]}$	+	−	0	−	−	$2\tau_1+t_1$	$2\tau_2-t_2$
$dPE_{[12p]3}$	+	0	+	−	−	$3\tau_1+\tau_2+t_1$	$-\tau_1+\tau_2-t_2$
$dPE_{1[2p\,p']}$	+	−	0	0	−	$2\tau_1+t_1+t_2$	$2\tau_2-2t_2$
$dPE_{[12p]p'}$	+	0	+	+	−	$3\tau_1+\tau_2+t_1+2t_2$	$-\tau_1+\tau_2-3t_2$
$dPE_{1[23p']}$	+	−	−	0	−	$2\tau_1+t_2$	-
$dPE_{[123]p'}$	+	0	0	+	−	$3\tau_1+\tau_2+2t_2$	-
$dPE_{1[p3p']}$	+	+	−	0	−	$4\tau_1+2\tau_2-2t_1+t_2$	$\tau_1-\frac{1}{2}t_2$
$dPE_{[1p3]p'}$	+	+	0	+	−	$4\tau_1+2\tau_2-t_1+2t_2$	$2\tau_1+t_2$
$dPE_{2[p3p']}$	0	+	−	0	−	$3\tau_1+2\tau_2-2t_1+t_2$	$\frac{1}{2}\tau_1-\frac{1}{2}t_2$
$dPE_{[2p3]p'}$	0	+	0	+	−	$3\tau_1+2\tau_2-t_1+2t_2$	τ_1+t_2
$dPE_{[12p]3}r_{p'}$	−	0	−	+	−	$\tau_1+\tau_2-t_1+2t_2$	$-\tau_1-\tau_2+t_2$
$dPE_{1[2p3]}r_{p'}$	−	+	0	+	−	$2\tau_1+2\tau_2-t_1+2t_2$	t_2
$dPE_{12}r_{[p3p']}$	−	+	−	0	−	$2\tau_1+2\tau_2-2t_1+t_2$	$-\frac{1}{2}t_2$
SE_{12p}	+	0	−	−	−	$3\tau_1+\tau_2-t_1$	$\tau_1-\tau_2-t_2$
SE_{123}	+	0	0	−	−	$3\tau_1+\tau_2$	-
$SE_{12p'}$	+	0	0	0	−	$3\tau_1+\tau_2+t_2$	-
SE_{1p3}	+	+	0	−	−	$4\tau_1+2\tau_2-t_1$	$2\tau_1-t_2$
$SE_{1p\,p'}$	+	+	0	0	−	$4\tau_1+2\tau_2-t_1+t_2$	$2\tau_1$
$SE_{13p'}$	+	+	+	0	−	$4\tau_1+\tau_2+t_2$	-
SE_{1p3}	0	+	0	−	−	$3\tau_1+2\tau_2-t_1$	τ_1-t_2
$SE_{2p\,p'}$	0	+	0	0	−	$3\tau_1+2\tau_2-t_1+t_2$	τ_1
$SE_{23p'}$	0	+	+	0	−	$3\tau_1+2\tau_2+t_2$	-
$SE_{p3p'}$	0	0	+	0	−	$2\tau_1+\tau_2+t_1+t_2$	τ_2-2t_2
$SE_{12p}r_3$	−	0	+	−	−	$\tau_1+\tau_2+t_1$	$\tau_1+\tau_2-t_2$
$SE_{123}r_{p'}$	−	0	0	+	−	$\tau_1+\tau_2+2t_2$	-
$SE_{12p}r_{p'}$	−	0	+	+	−	$\tau_1+\tau_2+t_1+2t_2$	$\tau_1+\tau_2-3t_2$
$SE_{1p3}r_{p'}$	−	−	0	+	−	t_1+2t_2	$2\tau_1+2\tau_2-3t_2$
$SE_{2p3}r_{p'}$	0	−	0	+	−	$\tau_1+t_1+2t_2$	$\tau_1+2\tau_2-3t_2$
$SE_{12p}r_3r_{p'}$	+	0	−	+	−	$3\tau_1+\tau_2-t_1+2t_2$	$\tau_1-\tau_2+t_2$
$SE_{(PE12)p3}$	−	+	0	−	−	$2\tau_1+2\tau_2-t_1$	$-t_2$
$SE_{(PE12)3p'}$	−	+	+	0	−	$2\tau_1+2\tau_2+t_2$	-
$SE_{(PE12)p\,p'}$	−	+	0	0	−	$2\tau_1+2\tau_2-t_1+t_2$	0
$SE_{(PE1p)3p'}$	−	−	+	0	−	$2t_1+t_2$	$\tau_1+\tau_2-\frac{3}{2}t_2$
$SE_{(PE2p)3p'}$	0	−	+	0	−	$\tau_1+2t_1+t_2$	$\frac{1}{2}\tau_1+\tau_2-\frac{3}{2}t_2$
$SE_{(PE12)p3}r_{p'}$	+	−	0	+	−	$2\tau_1+t_1+2t_2$	$2\tau_2-3t_2$
$SE_{(PE12rp)3p'}$	+	−	+	0	−	$2\tau_1+2t_1+t_2$	$\tau_2-\frac{3}{2}t_2$
$SE_{(SE12p)3p'}$	−	0	+	0	−	$\tau_1+\tau_2+t_1+t_2$	$\tau_1+\tau_2-2t_2$
$dSE_{12[p3p']}$	+	0	−	0	−	$3\tau_1+\tau_2-t_1+t_2$	$\tau_1-\tau_2$
$dSE_{[12p]3p'}$	+	0	+	0	−	$3\tau_1+\tau_2+t_1+t_2$	$-\tau_1+\tau_2-2t_2$

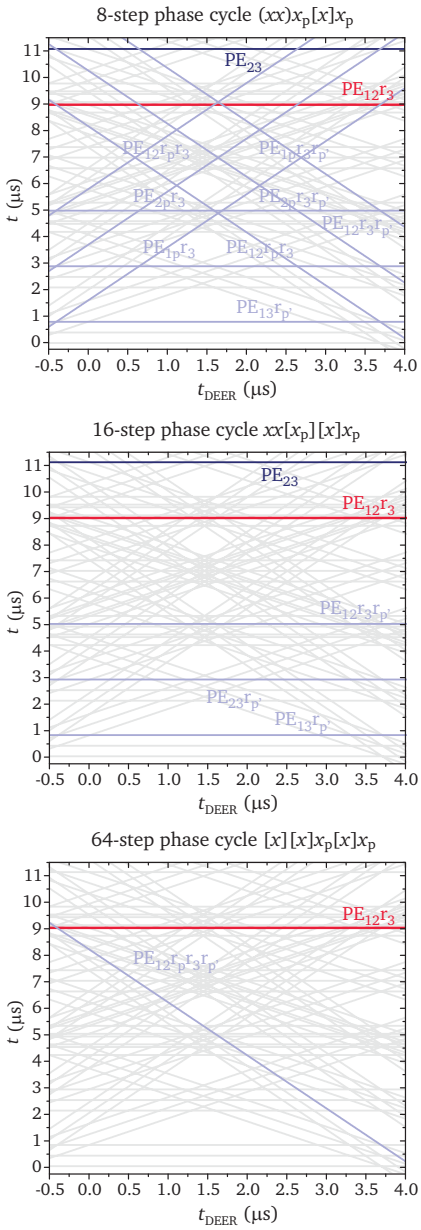

Fig. S15 Visualization of the echoes removed in different phase cycles for reverse five-pulse DEER. The positions of the echo crossings in a five-pulse DEER experiment with $\tau_1 = 2.1\,\mu s$, $\tau_2 = 2.4\,\mu s$ and $t_2 = 400\,ns$ are shown as in Fig. 8. The lines corresponding to echoes removed by the phase cycle are shown in grey, the detected echo is shown in red, and the echoes not removed by phase cycling are shown in different shades of blue depending on the type of echo and are labelled according to Table S2.

4.2 Seven-pulse DEER

The potentially interfering echoes not removed by different phase cycles in the seven-pulse DEER experiment are listed in Table S3 along with the corresponding refocusing times. The corresponding echo positions during the DEER experiment are plotted in Fig. S16.

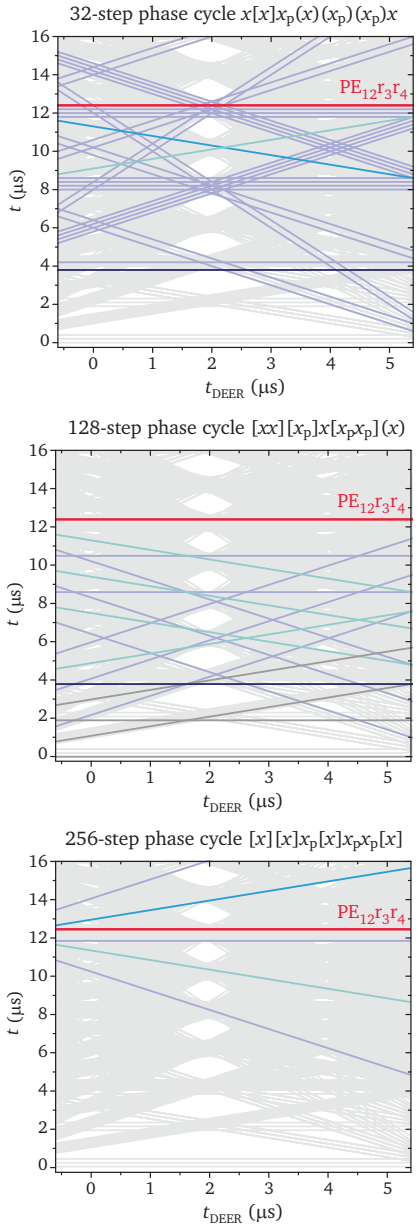

Fig. S16 Visualization of the echoes removed in different phase cycles for the seven-pulse DEER sequence. The positions of the echo crossings in a seven-pulse DEER experiment with $\tau_1 = 1.9\,\mu s$, $\tau_2 = 2.1\,\mu s$, $\tau_3 = 2.2\,\mu s$ and $t_2 = 200\,ns$ are shown as in Fig. 9. The lines corresponding to echoes removed by the phase cycle are shown in grey, the detected echo is shown in red, and the echoes not removed by phase cycling are shown in different shades of blue depending on the type of echo.

Table S3 List of echoes not removed by different phase cycling schemes in the seven-pulse DEER experiment (only standing echoes within τ_1 from the detected echo and moving echoes crossing within the range $0 \le t_{DEER} \le \tau_1+\tau_2+\tau_3-t_{1,0}-t_2-t_{3,0}$ are listed). The echoes, positions and distance $|t_{echo}-t_{PE_{12}r_3r_4}|$ between the echoes and the detected refocused echo for standing echoes, and the crossing times $t_{DEER,cross}$ with the refocused echo $PE_{12}r_3r_4$ for the moving echoes are given. (PE = primary echo, SE = stimulated echo, r = refocused, d = delayed). The time axis of the DEER experiment is given by $t_{DEER} = \tau_1+\tau_2+\tau_3-|t_1|-|t_2|-|t_3|$. The delays t_1 and t_3 are considered to be equal.

32-step phase cycle $x[x]x_{\mathbf{p}}(x)(x_{\mathbf{p}})x$

Echo	Position	$\lvert t_{echo}-t_{PE_{12}r_3r_4}\rvert$
$PE_{12}r_{p''4}$	$2(\tau_1+\tau_2+\tau_3-t_2)$	$-2t_2$
$PE_{12}r_{p'},r_3r_{p'''}r_4$	$2(2\tau_1+\tau_2)$	$2(\tau_1-\tau_3)$
$PE_{12}r_{p'},r_{p''}r_{p'''}r_4$	$2(2\tau_1+\tau_2+t_2)$	$2(\tau_1-\tau_3+t_2)$
Echo	Position	$t_{DEER,cross}$
$PE_{12}r_{p'''}$	$2(\tau_1+2\tau_2+\tau_3-2t_1)$	$\tau_1-\tau_2+\tau_3-t_2$
$PE_{12}r_{p'},r_{p'''}$	$2(2\tau_1+2\tau_2+\tau_3-2t_1)$	τ_3-t_2
$PE_{12}r_{p'},r_3r_4$	$2(\tau_2+\tau_3+t_1)$	$-\tau_1+\tau_2+\tau_3-t_2$
$PE_{12}r_{p'},r_{p''}r_4$	$2(\tau_2+\tau_3+t_1-t_2)$	$-\tau_1+\tau_2+\tau_3-3t_2$
$PE_{12}r_3r_{p''}r_{p'''}$	$2(\tau_1+2\tau_2+\tau_3-t_1-t_2)$	$\tau_1-\tau_2+\tau_3+t_2$
$PE_{12}r_3r_{p'''}r_4$	$2(\tau_1+\tau_2+t_1)$	$\tau_1+\tau_2-\tau_3-t_2$
$PE_{12}r_{p''}r_{p'''}r_4$	$2(\tau_1+\tau_2+t_1+t_2)$	$\tau_1+\tau_2-\tau_3+t_2$
$PE_{12}r_{p'},r_3r_{p''}r_{p'''}$	$2(2\tau_1+2\tau_2+\tau_3-2t_1-t_2)$	τ_3
$PE_{12}r_{p'},r_3r_{p''}r_{p'''}r_4$	$2(2t_1+t_2)$	0

128-step phase cycle $[xx][x_{\mathbf{p}}]x[x_{\mathbf{p}}x_{\mathbf{p}}](x)$

Echo	Position	$\lvert t_{echo}-t_{PE_{12}r_3r_4}\rvert$
$PE_{23}r_4$	$\tau_1+2\tau_2+2\tau_3$	τ_1

256-step phase cycle $[x][x]x_{\mathbf{p}}[x]x_{\mathbf{p}}x_{\mathbf{p}}[x]$ **(observer only)**

Echo	Position	$\lvert t_{echo}-t_{PE_{12}r_3r_4}\rvert$
$PE_{12}r_{p'},r_3r_{p'''}r_4$	$2(2\tau_1+\tau_2)$	$2(\tau_1-\tau_3)$

References

1 A. Doll, S. Pribitzer, R. Tschaggelar and G. Jeschke, *J. Magn. Reson.*, 2013, **230**, 27–39.

2 P. E. Spindler, Y. Zhang, B. Endeward, N. Gershernzon, T. E. Skinner, S. J. Glaser and T. F. Prisner, *J. Magn. Reson.*, 2012, **218**, 49–58.

3 A. Doll, M. Qi, N. Wili, S. Pribitzer, A. Godt and G. Jeschke, *J. Magn. Reson.*, 2015, **259**, 153–162.

4 P. E. Spindler, S. J. Glaser, T. E. Skinner and T. F. Prisner, *Angew. Chem. Int. Ed.*, 2013, **52**, 3425–3429.

5 H. A. DeBerg, J. R. Bankston, J. C. Rosenbaum, P. S. Brzovic, W. N. Zagotta and S. Stoll, *Structure*, 2015, **23**, 734–744.

6 G. Jeschke, S. Pribitzer and A. Doll, *J. Phys. Chem. B*, 2015, **119**, 13570–13582.